Impact of Preheating on Flame Stabilization and NOx Emissions From a Dual Swirl Hydrogen Injector

Hervé Magnes, Sylvain Marragou, Andrea Aniello, Laurent Selle, Thierry Poinsot, Thierry Schuller

IMPACT OF PREHEATING ON FLAME STABILIZATION AND NOX EMISSIONS FROM A DUAL SWIRL HYDROGEN INJECTOR

Hervé Magnes*, Sylvain Marragou, Andrea Aniello, Laurent Selle, Thierry Poinsot, Thierry Schuller
Institut de Mécanique des Fluides de Toulouse, IMFT, Université de Toulouse, CNRS, Toulouse, France

ABSTRACT

Flame stabilization, flame structure and pollutant emissions are investigated experimentally on a swirled injection system operating with globally lean air/hydrogen mixtures at atmospheric conditions and moderate Reynolds numbers. This injector consists of two coaxial ducts with separate injection of hydrogen into a central channel and of air into an annular channel. Both streams are swirled. The resulting flames exhibit two stabilization modes. In one case, the flame takes an M-shape and is anchored to the hydrogen injector lips. In the second case, the flame is aerodynamically stabilized above the injector and takes a V-shape. Regions of existence of each stabilization mode are determined according to the operating conditions. For low air flow rates, the flame can be either anchored or lifted above the hydrogen injector lips depending on the path followed to reach the operating condition. At high air flow rates, the flame is always lifted regardless of the trajectory followed. The impact of air inlet temperature on these stabilization regimes is then evaluated from $T = 300$ K up to 770 K. Flame re-attachment is shown to be controlled by edge flame propagation and the impact of preheating is well reproduced by the model. Unburnt hydrogen and NO_x emissions are finally evaluated. Unburnt hydrogen is only observed for global equivalence ratios below 0.4 and at ambient inlet temperature. NO_x emissions decrease when the global equivalence ratio is reduced. Furthermore, at fixed global equivalence ratio, NO_x emissions decrease as the thermal power increases, regardless of air preheating and the flame stabilization regime. At high power, NO_x emissions reach an asymptotic value that is independent of the thermal power. The impact of flame shape, air preheating and combustion chamber wall heat losses on NO_x production is also evaluated. NO_x emissions are shown to scale with the adiabatic flame temperature T_{ad} at the global equivalence ratio and the residence time inside the combustor.

INTRODUCTION

Hydrogen is a promising fuel to achieve the decarbonization of the energy sector and an attractive solution to reduce the environmental impact of both aeronautical and land-based gas turbines. Although widely used in rocket propulsion, hydrogen combustion in gas turbines applications remains controversial. H_2 exhibits higher molecular diffusivity, greater laminar burning velocity, larger flammability limits and lower activation energy than standard hydrocarbons [1]. These characteristics increase the risk of spontaneous ignition and flashback in premixed systems, raising important safety concerns [2].

For these reasons, current H_2 technologies are mainly based on separate injection of reactants [3]. Nevertheless, this approach promotes the formation of diffusion-controlled flames that, exhibiting higher flame temperatures, produce greater NO_x emissions [4]. Hence, it is necessary to develop combustion systems that simultaneously limit this NO_x production and comply with safety standards.

In this respect, several approaches have been proposed and a comprehensive review of the technologies currently developed was proposed by Du Toit *et al*. [5]. It emerges that Dry Low NO_x (DLN) technologies are the most widely accepted because they guarantee higher efficiency and durability. One example of DLN strategy is based on Lean Direct Injectors (LDI), which are designed to provide a late injection of fuel into the combustion chamber to avoid flashback on one side, and favor mixing between reactants to mitigate NO_x emissions on the other side. This is the strategy used in Micromix Injection Systems (MMI), which consists on dividing the main fuel and air streams into a multitude of small nozzles distributed all over the combustion chamber backplane, leading to a collection of small flames. Many versions of MMI can be found, which differ mainly by the fuel injection system adopted: micro swirl-based injection [6, 7] or jet in cross-flow injection [8–10]. Even though MMI technologies

*Corresponding author : herve.magnes@imft.fr

enable to reduce NO_x emissions [11], they require substantial modifications of the combustion chamber architecture, raising many challenges in terms of design, manufacturing and implementation. Moreover, Funke *et al.* [8] showed that to achieve safe and reliable nominal engine operation, specific procedures must be followed limiting the operability range of the engine. For instance, the M1A Micromix prototype requires a variable control of the injection zone to ensure flame stability during the ignition sequence [8].

These limitations make conventional swirl burners an appealing solution to design non-premixed systems because of the established know-how, the flexible control and their easier implementation in current combustion chamber architectures. Moreover, swirl flows are a well-known versatile solution to stabilize aerodynamically flames [12], limit flame blow-off [13] and reduce NO_x emissions [14] thanks to the mixing enhancement between reactants. Recent experimental and numerical investigations conducted with swirl burners powered by H_2 are mostly dedicated to premixed [15, 16] or technically-premixed systems [17]. Cheng *et al.* [18], for instance, adopted a conventional premixed low swirled burner fueled with H_2 demonstrating that, despite its good performances in terms of emissions, premixed systems remain subjected to flame anchoring and flashback issues.

To counter these negative aspects and keep advantage of swirl injectors, an alternative system is proposed in this study. The HYdrogen LOw NO_x injector (HYLON) is developed at IMFT laboratory in collaboration with Safran Helicopter Engine [19]. It consists of two swirled coaxial ducts to keep the reactants separated upstream the combustion chamber [20]. As demonstrated by Yuasa *et al.* [21], co-swirling fuel and air streams promotes flame lifting.

Degeneve *et al.* [22, 23] adopted a similar double-swirled injector to stabilize oxy-methane flames, putting in evidence several flame stabilization regimes depending on the impulsion ratio between the fuel and air streams. The same burner was exploited by Leroy *et al.* [24] to investigate NO_x productions from H_2-air flames. In the meantime, Marragou *et al.* [20] conducted a geometrical parametric study on a coaxial swirled injector for H_2-enriched flames. It was shown that a small recess between the hydrogen injector lip and the chamber backplane enables to widen the burner operability range leading to lifted flames. In the last two studies [20, 24], the chosen injection strategies lead to controlled NO_x emissions for a variety of operating conditions and two main stabilization modes were identified: flames anchored to the hydrogen nozzle and aerodynamically stabilized flames.

A recent numerical study from Aniello *et al.* [25] considers the HYLON injector and scrutinizes the flame structure and the stabilization mechanisms for the aforementioned regimes. They showed that H_2 attached flames are entirely governed by diffusion, while lifted flames present a central diffusion branch accompanied by a lateral partially premixed flame wing. Hence, the flame stabilization mode, the air and hydrogen injections velocities, alter the NO_x emissions. More recently, Marragou *et al.* [26] identified the edge flame displacement of the diffusion branch as the controlling mechanism for flame re-anchoring that was also corroborated by numerical flow simulations [25].

The present work investigates an evolution of the HYLON injector with a new optimized geometry enabling to (1) augment the injection velocities by reducing pressure losses and (2) further widen its operability with lifted flames. The test rig is not designed to sustain high pressure, but air can be preheated to get closer to engine-like operating conditions. The objectives are to expand the range of operating conditions tested in previous studies and evaluate the impact of air pre-heating temperature on flame structure, flame stabilization, and NO_x emissions.

The experimental setup is described in the next section, followed by a parametric analysis of flame stabilization with a focus on the impact of air preheating. Finally NO_x emissions are considered for ambient and preheated conditions before conclusions are drawn.

EXPERIMENTAL SETUP

Figure 1(a) shows the test rig and the HYLON burner, which is an optimized version of the one investigated in [20, 25, 26]. The test bench is used to stabilize H_2-air swirled flames with the objective to minimize the pressure losses through the injector and the range of operating conditions with lifted flames. The mass flow rates of air and hydrogen are regulated via two Brooks SLA 585x series mass flow controllers. Dry air is supplied at the bottom of the plenum and goes through a LEISTER 5000-DF heater, which is used in the study to control the air injection temperature inside the combustion chamber. The pre-heated air passes through a cylindrical plenum and through a convergent section. It then penetrates the annular channel of the injector with an external diameter $d_e = 18$ mm. Hydrogen is injected at ambient conditions via a central lance of internal diameter $d_i = 6$ mm, coincident with the central axis of the burner. A close up of the HYLON injector cross section is presented in Fig. 1(b). The annular nozzle is equipped with a radial to axial swirl vane shown in Fig. 1(c) that produces a swirl number $S_e = 0.9$ estimated with geometrical considerations. The internal H_2 nozzle, instead, embeds an axial swirler shown in Fig. 1(d), which generates a swirl number $S_i = 0.6$. Figure 1(b) also highlights an injector recess $z_i = 6$ mm corresponding to the distance between the chamber backplane and the top of the hydrogen injection tube that favors mixing between reactants upstream the combustion chamber. The lip of the hydrogen nozzle features a 45° chamfer that increases the H_2 tube external diameter from 10 mm to 12 mm. The flame is confined in a square combustion chamber, which is made of four quartz windows to provide full optical access to the reaction zone. The combustion chamber has a square cross section of $d_q = 78$ mm width and $L_q = 150$ mm length. It also

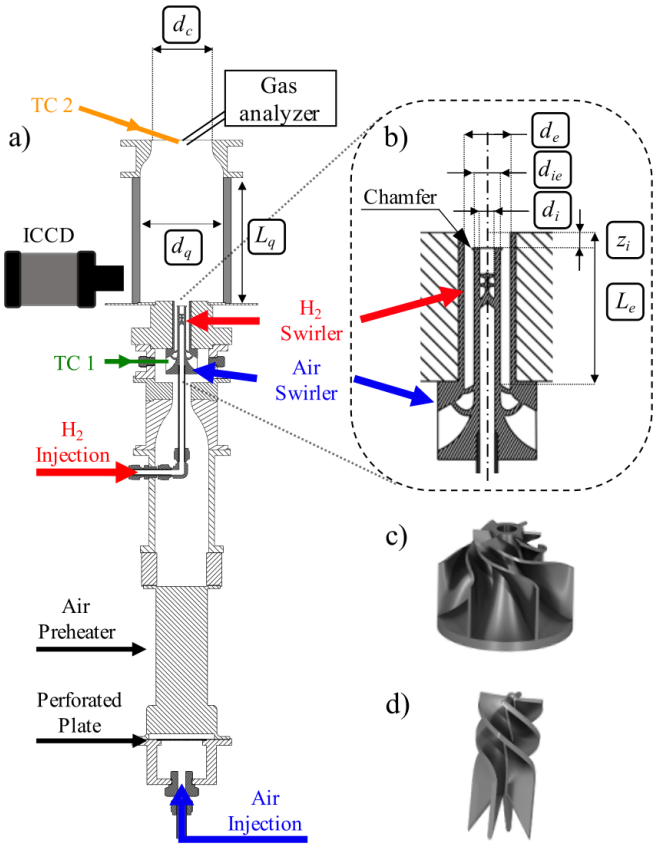

FIGURE 1: Diagram of the HYLON bench containing a LEISTER 5000DF preheater (a), with a close up of the injector geometry (b) and pictures of the radial-axial air swirler (c) and axial H_2 swirler (d).

features a reduced outlet section of diameter $d_c = 73$ mm to prevent engulfment of external air inside the combustion chamber.

A 50 mm-thick refractory ceramic fiber envelope can also be added around the combustion chamber to limit the wall heat losses. The temperature of the burnt gases T_{gb} is measured by a double bead thermocouple coupled to the Reduced Radiation Error technique [27]. Temperatures were measured at different locations at the combustion chamber outlet and show very similar results except near the walls. Only the temperature T_{gb} in the center of the outlet section is presented.

Mean flame images are collected in the visible band with a Nikon D7500 with a lens Nikon AF-S VR Micro-Nikkor 105 mm f/2.8G IF-ED or with a Princeton PIMAX-4 intensified CCD camera equipped with a 105 mm f/4.5 Nikon Rayfact UV-105 lens. For the latter, a narrow band filter ASAHI XHQA310 centered at 310±10 nm is used to isolate the OH^* signal peak emission, which is used as qualitative marker for the heat release rate [28].

Emissions are measured with an ECOM J2KN Pro flue gas analyzer with a probe collector located at the outlet of the combustor chamber on the centerline as indicated in Fig. 1(a). Additional samples were also made at different radial locations, with and without the probe collector cooling, without showing substantial differences. The NO and NO_2 concentrations of the sampled dried flue gases are given with a confidence interval of ±5% with respect to the measured value. Data are here only reported as NO_x without distinguishing between NO and NO_2.

FLAME STABILIZATION

The different regimes obtained with this new version of the HYLON burner are reported in the stabilization map in Fig. 2 when air is injected at ambient temperature. Results are presented as a function of the mass flow rate of hydrogen $\dot{m}_{H_2}$ and mass flow rate of air $\dot{m}_{air}$. Iso-values of the global equivalence ratio are also reported as black lines from $\phi_g = 0.1$ to $\phi_g = 1.0$. The blue square markers in Fig. 2 represent the operating conditions that separate three zones corresponding to different stabilization regimes.

Zone 1 occupies the bottom left side of the map and is observed for low mass flow rates of air and hydrogen. This regime always results in anchored flames, such as the one shown in Fig. 3(a). This flame archetype was already observed in the previous version of the burner [20, 25].

Zone 2 is observed for higher fuel mass flow rates $\dot{m}_{H_2}$ than Zone 1 and for air mass flow rates $\dot{m}_{air}$ higher than 1.3 g/s for this geometrical configuration of the HYLON injector. In this regime a dual stabilization mode is observed for the same operating conditions, with anchored or lifted flames depending either on the path followed to reach the operating point or on the ignition procedure adopted. For instance, Figs. 3(b-c) show anchored and lifted flames for the same reactants mass flow rates: $\dot{m}_{air} = 3.46$ g/s and $\dot{m}_{H_2} = 0.05$ g/s. Flames belonging to Zone 1 and Zone 2 were already investigated in [20, 25] for gases injected at ambient conditions. It was shown that the transition from lifted to anchored flames, i.e. from Zone 2 to Zone 1, is controlled by the propagation of an edge flame [26]. To identify the H_2 threshold velocity at which this transition takes place, the H_2 injection mass flow rate is gradually reduced until the sudden transition to an attached flame belonging to Zone 1.

Zone 3 is reached for air mass flow rates higher than roughly $\dot{m}_{air} = 5.0$ g/s, quasi-independently of the H_2 content. The threshold air velocity is determined by gradually increasing the air mass flow rate starting from an anchored flame in Zone II (e.g. Flame B). In this regime, the flame is unconditionally lifted regardless the path followed to reach the selected operating condition, except for very low hydrogen mass flow rates corresponding to the red color region at the bottom of the chart. An example of lifted flame in this regime is reported in Fig. 3(d). When the hydrogen mass flow rate is reduced, a reaction layer gradually

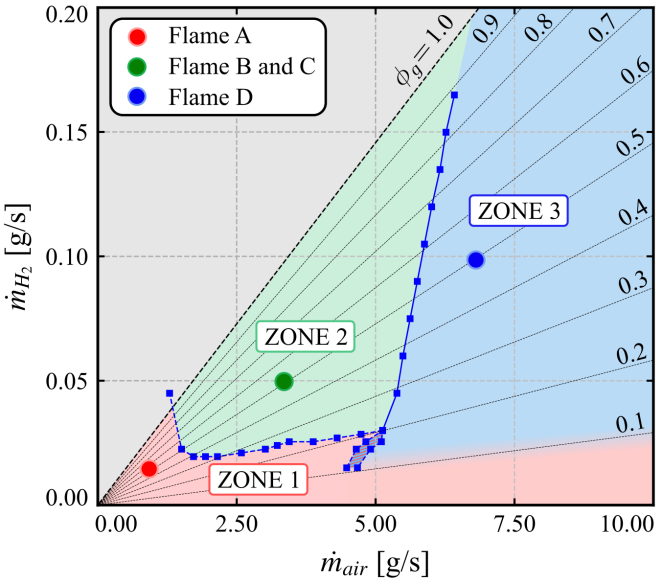

FIGURE 2: Stabilization map identifying three zones that correspond to different flame stabilization regimes gathered for ambient air inlet temperature.

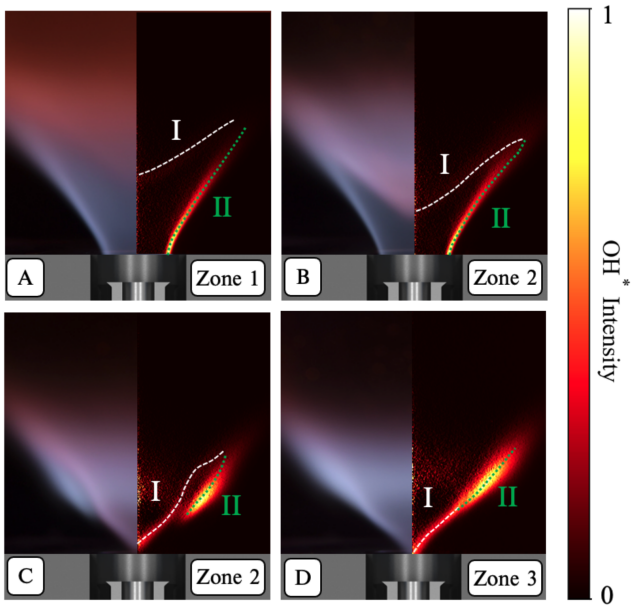

FIGURE 3: Flame images corresponding to different stabilization regimes. Left: Direct visualization in the visible band. Right: Inverse Abel transformed OH* images. (a) Anchored flame in Zone 1. (b) Anchored flame in Zone 2. (c) Lifted flame in Zone 2. (d) Lifted flame in Zone 3. Operating conditions are given in Tab. 1.

approaches closer to the hydrogen nozzle rim an eventually ends up to re-attach to the burner rim. This transition is smooth and does not feature any hysteresis: when the hydrogen flow rate is re-increased the flame also progressively detaches from the hydrogen nozzle rim for the same conditions as those observed for flame anchoring to the nozzle. This smooth transition free of any hysteresis contrasts with the abrupt switch from lifted flames in Zone 2 to attached flames in Zone 1 as studied in [26] when the hydrogen flow rate is reduced. The transition from Zone 1 to Zone 3, and conversely from Zone 3 to Zone 1, is intermittent with a flame randomly switching between the two stabilization modes.

Figures 3(a-d) show four mean flame images corresponding to the operating conditions described in Tab. 1 and highlighted by the colored disks in Fig. 2. The left-hand side of each image corresponds to the visible light recorded by a standard camera. The right-hand sides result from Abel deconvolution of the line of sight integrated OH* signal. They are used to infer the location of the different reaction layers in the axial plane of the burner.

Figures 3(a-b) correspond to attached flames A and B belonging to Zones 1 and 2 respectively. These flames feature the same global equivalence ratio ϕ_g but different thermal powers $\mathscr{P}_{th}$. They both have an M-shape characterized by two main branches. The lateral one, denoted II and delimited by dotted lines in Figs. 3, penetrates inside the injector and stabilizes on the hydrogen injection tube lips. The flame root protruding inside the metallic burner is in these cases not visible. Reaction layer II is a diffusion reaction front between the air and hydrogen flows exhausting from the burner as shown in [25]. This reaction layer appears as a blue wing in the visible range, while the normalized OH* signal distribution suggests that the reaction rate is more intense near the chamber backplane and reduces further

TABLE 1: List of operating conditions for the flames reported in Fig. 3. The bulk flow velocities $u_{b,air}$ inside the air channel and $u_{b,H2}$ inside the hydrogen channel are at ambient temperature.

Flame	A	B and C	D
$\dot{m}_{air}$ [g/s]	1.15	3.46	6.92
$\dot{m}_{H_2}$ [g/s]	0.02	0.05	0.10
$u_{b,air}$ [m/s]	5.6	16.9	33.8
u_{b,H_2} [m/s]	7.3	21.8	43.6
ϕ_g	0.5	0.5	0.5
$\mathscr{P}_{th}$ [kW]	2	6	12

away. The central branch, instead, is delimited by dashed lines and noted I in Figs. 3. Branch I develops in the shear layer between the hydrogen central jet exhausting from the burner and the hot gases inside the Central Recirculation Zone (CRZ). The weak reaction layer I in Figs. 3(a-b) has a reddish color in the visible bandwidth corresponding to the chemiluminesence of hot H_2O^* radicals [29]. The normalized OH^* signal is much weaker along the reaction front I than along the lateral branch II in Figs. 3(a-b).

It was shown in [25] that flames A and B are entirely controlled by diffusion processes. Figures 3(a-b) reveal however some differences. For instance, the OH^* signal indicates that the apex of the central branch I of flame B is closer to the injector outlet than in flame A. This difference is due to the different intensity of the CRZ when the mass flow rates of reactants are increased. Moreover, while the distributions of the reaction rate are similar in the two cases, the thickness of the OH^* footprint for the lateral branch II is narrower for flame B than for flame A. This observation corroborates the diffusion nature of this reaction layer. Flame B is subject to a higher strain rate due to higher air and hydrogen flow injection velocities leading to a reduction of the thickness of the reaction zone.

Flames B and C in Figs. 3(b-c) are now considered. They both can be found in Zone 2 and are obtained for the same injection conditions (see Tab. 1), but flame B is anchored to the hydrogen nozzle while flame C is lifted. The main difference between flames B and C is that the lateral branch II from flame C is detached from the hydrogen injector lips and stabilizes a few millimeters above the chamber backplane. Concomitantly, the central branch I in flame C is pushed closer to the injector outlet, as highlighted by the position of the dashed line in Fig. 3(c). Since the lateral branch II moves downstream and the central branch I stabilizes upstream, the two reaction layers get closer to each other with respect to the attached flames A and B, in which cases the reaction layers I and II are well separated. Furthermore, the normalized OH^* intensity of the apex of the central reaction layer I from the lifted flame C in Fig. 3(c) lying on the symmetry axis of the burner takes now much higher values than the apex of the central branch I for the anchored flame B shown in Fig. 3(b). Simultaneously, the highest normalized OH^* intensity reached along the reaction layer II shifts downstream with respect to flame B. While branches I and II from flame B are entirely dominated by diffusion reactions, the lifted branch II from flame C lies far from the hydrogen and air injector nozzles. Partial mixing takes place between the reactants before combustion and branch II is a partially premixed flame as confirmed in [25]. This is the main reason why lifted flames produce less NO_x than attached flames [20].

Flames C and D in Figs. 3(c-d) are finally compared. They share the same global equivalence ratio ϕ_g but the thermal power $\mathscr{P}_{th}$ is the double for flame D (see also Tab. 1). Doubling the reactant velocities, the flame length slightly increases from flame C to D and the location of the maximum reaction rate is pushed further downstream along the dotted line on the right in Fig. 3(d). Interestingly, the left image in Fig. 3(d) also indicates that the flame branch I looses the reddish color from hot H_2O^* emission for the other operating conditions in Fig. 3(a-c). This suggests that the temperature along branch I is cooler for Flame D compared to previous operating conditions. Moreover, the lateral branch II and the central branch I cannot be distinguished anymore for flame D. The upstream displacement of the central flame branch I observed during the transition from flame B to C, is exacerbated in flame D, and the two branches I and II have merged. This again is corroborated by the simulations conducted in [25] for different operating conditions. These experiments prove that at high flow rates, the central diffusion reaction layer I and the lateral partially premixed reaction layer II merge together leading to a unique lifted reaction layer with a diffusion structure at the flame apex lying on the burner symmetry axis and a mixture composition gradient along the wings of the flame brush.

TABLE 2: The ratio between the mass of the remaining H_2 in exhaust gases and the total mass of hydrogen injected (H_2 [%]) is presented as function of three globally lean equivalence ratios ϕ_g and several input thermal powers $\mathscr{P}_{th}$. Data are presented for ambient air inlet temperature $T_{air,in} = T_{amb}$.

	$\mathscr{P}_{th}$ [kW]	2	4	5	8	12	15
$\phi_g = 0.4$	H_2 [%]	0.00	0.00	0.00	0.00	0.00	0.00
	F. Shape	Anc.	A/L	A/L	Lift	Lift	Lift
$\phi_g = 0.3$	H_2 [%]	0.00	0.00	0.19	0.15	0.04	0.00
	F. Shape	Anc.	Anc.	Lift	Lift	Lift	Lift
$\phi_g = 0.2$	H_2 [%]	0.11	2.49	3.20	3.54	4.96	/
	F. Shape	Anc.	Lift	Lift	Lift	Lift	/

Another interesting feature is that blow-off could not be reached for all the operating range which was tested, even at very lean injection conditions $\phi_g < 0.1$. This is due to the separate injection of air and hydrogen yielding always a stoichiometric zone close to the central injector outlet, even for very low hydrogen flow rates. However, injection of hydrogen at very lean conditions $\phi_g \leq 0.3$ results in incomplete combustion with unburnt H_2 remaining in the exhaust gases, as indicated in Tab. 2. At $\phi_g = 0.3$, low levels of unburnt H_2 are only observed at low thermal power. Hence, although anchored flames are generally undesirable, they favor a better combustion efficiency. When $\phi_g < 0.3$, the H_2 concentration in the burnt gases remains high, regard-

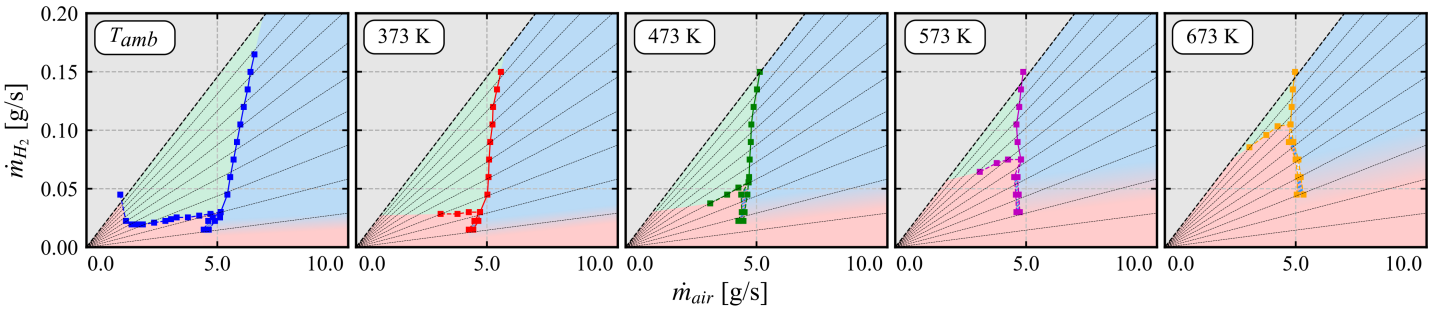

FIGURE 4: Flame stabilization maps obtained with the HYLON injector for different levels of air preheating: from ambient temperature to $T_{air,in}$ = 673 K. Red: Zone I. Green: Zone II. Blue: Zone III.

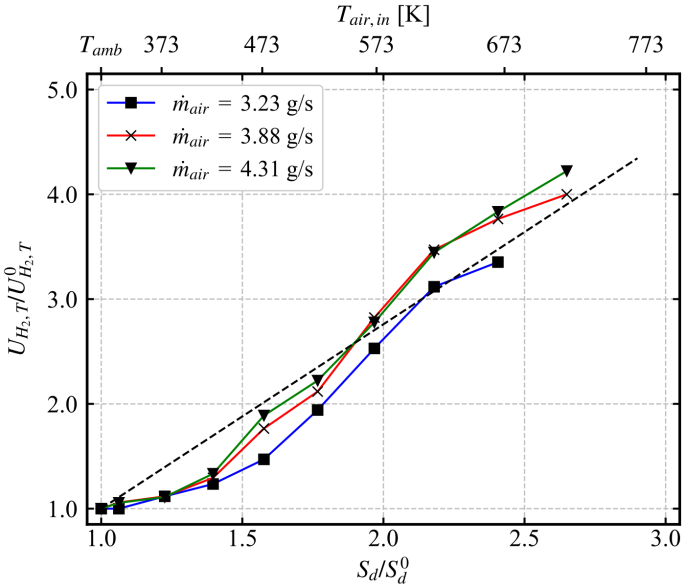

FIGURE 5: Evolution of the H_2 bulk velocity $U_{H_2,T}$ corresponding to the transition between Zone 2 and Zone 1 with respect to the edge flame velocity S_d calculated from CANTERA 1D simulations according to Eq. (1). Both variables are normalized by their values $U^0_{H_2,T}$ and S^0_d at ambient temperature.

less of the thermal power. For $\phi_g \geq 0.4$, combustion is always complete even at ambient air injection temperature. It should be noted that these measurements were conducted at ambient air inlet temperature $T_{air,in} = T_{amb}$. Concentrations of unburned H_2 drastically drop with air preheating.

IMPACT OF AIR PRE-HEATING

In a gas-turbine, air is compressed before entering the combustion chamber and its injection temperature can reach up to $T_{air,in} = 950$ K. Hence, from technical perspective it is necessary to assess the impact of the thermodynamic inlet conditions on the stabilization chart shown in Fig. 2, which was obtained by injecting air at ambient temperature. The effect of the air preheating is analyzed in Fig. 4, while the impact of increasing pressure is left for further studies. The boundaries between Zone 1, Zone 2 and Zone 3 are only reported for air mass flow rates higher than $\dot{m}_{air} = 3.2$ g/s, which is the minimum required to avoid overheating of the air preheater.

Increasing the air inlet temperature $T_{air,in}$ shifts the boundary between Zones 1 and 2 towards higher H_2 mass flow rates $\dot{m}_{H_2}$ and the boundary between Zones 2 and 3 to lower air mass flow rates $\dot{m}_{air}$. Hence, Zones 1 and 3 expand by increasing the air inlet temperature, while Zone 2 shrinks at high H_2 mass flow rates. As a consequence, Zone 2 exhibiting a dual stabilization mode disappears by increasing the air inlet temperature and the transition between lifted and anchored flames becomes predominantly driven by the air mass flow rate.

The shift of the boundary between the Zones 2 and 3 with air preheating can be further analyzed. A higher air inlet temperature increases the reactivity of the combustible mixture and this effect is expected to delay the lift-off of the flame. Nevertheless, Fig. 4 shows the opposite trend. This may be caused by the air volumetric flow rate that increases linearly with the inlet temperature $T_{air,in}$ for these experiments conducted at atmospheric conditions. For a fixed air mass flow rate, the increase of the air injection velocity overwhelms the greater reactivity of the mixture, thereby promoting the lifted stabilization regime. It is important to note that in a real engine, temperature and pressure are closely related. In such cases, an increase in the air bulk velocity due to the rise of the air inlet temperature would be partially balanced by the increase in density due to the rise in pressure, and the velocity field would remain roughly unchanged. Thus, the sensitivity of flame stabilization regime to the air inlet temperature may vary when both temperature and pressure are changed.

The shift of the boundary between Zone 1 and Zone 2 due

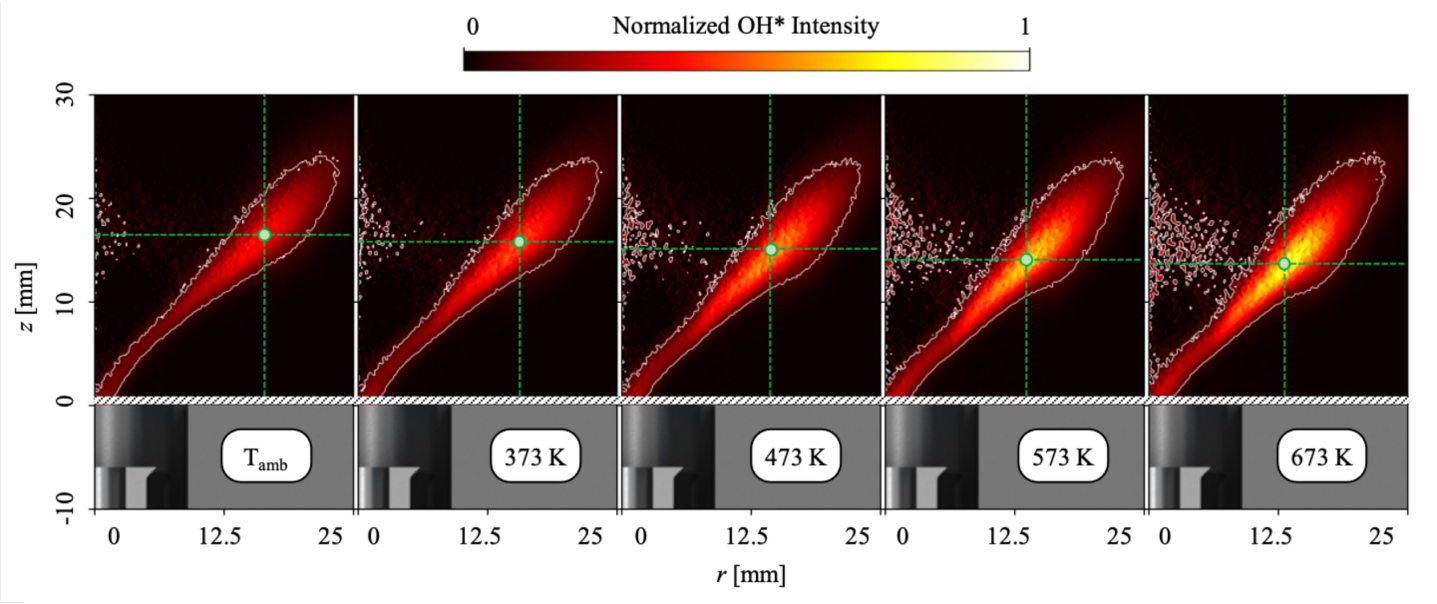

FIGURE 6: Inverse Abel transformed OH* images collected for the same input thermal power $\mathscr{P}_{th} = 18$ kW and same global equivalence ratio $\phi_g = 0.6$ and increasing air preheating temperature $T_{air,in}$ from ambient to 673 K.

TABLE 3: List of the operating conditions corresponding to the flame images shown in Fig. 6.

Temperature [K]	T_{amb}	373	473	573	673
$u_{b,air}$ [m/s]	42.1	51.8	65.6	79.5	93.4
u_{b,H_2} [m/s]	65.4	65.4	65.4	65.4	65.4
S_l [m/s] for $\phi_g = 0.6$	1.0	1.6	2.7	4.3	6.5

to the increase of the air preheating is now considered. Figure 5 shows how the hydrogen injection velocity leading to flame re-attachment, i.e. transition from Zone 2 to Zone 1, scales with the triple flame speed when air is preheated. Marragou *et al.* [26] showed that lifted flame re-attachment is driven by the propagation of an edge flame, which is capable of reaching the hydrogen injector lip when the leading edge flame speed S_d exceeds the local flow velocity along the most reactive mixture fraction line Z_{max} [30, 31]. The edge flame velocity along this line is estimated with:

$$S_d = S_{l,max} \left(\frac{\rho_u}{\rho_b} \right)^{1/2} \quad (1)$$

where $S_{l,max}$ corresponds to the maximum laminar burning velocity, and ρ_u/ρ_b is the volumetric expansion ratio of gases through the flame calculated for Z_{max} with Cantera 1D simulations. In Fig. 5, the hydrogen transition velocity $U_{H_2,T}$ and the edge flame speed S_d are both normalized by their respective values $U^0_{H_2,T}$ and S^0_d obtained at ambient conditions. Only the operating conditions belonging to the boundaries between Zones 1 and 2 observed at different air preheating are considered. Figure 5 indicates that an increase in S_d due to higher air preheating corresponds to a proportional increase in $U_{H_2,T}$, which extends Zone I. This proportional relationship between the two parameters supports the flame re-anchoring mechanism identified in [26]. In this analysis, H_2 which is injected at ambient temperature is assumed to be unaltered by air preheating.

The impact of $T_{air,in}$ on the shape taken by a flame belonging to Zone 3 is illustrated in Fig. 6. The normalized OH* distribution in the axial plane of the burner is presented for five flames characterized by an equivalence ratio $\phi_g = 0.6$, thermal power $\mathscr{P}_{th} = 18$ kW and different air inlet temperatures from $T_{air,in} = T_{amb}$ to $T_{air,in} = 673$ K. The air volumetric flow rate increases linearly with temperature, while the hydrogen flow rate is kept constant. Values for $u_{b,air}$ and u_{b,H_2} at different air inlet temperatures are given in Tab. 3.

The green markers correspond to the maximum OH* intensity for each operating condition. The position of the markers moves slightly closer to the injector outlet when the air inlet temperature $T_{air,in}$ increases, unveiling a small shortening of the flame due to air preheating. The reactivity of the mixture increases and the flame becomes more compact. This is in agreement with the intensity of the OH* signal that rises regularly with

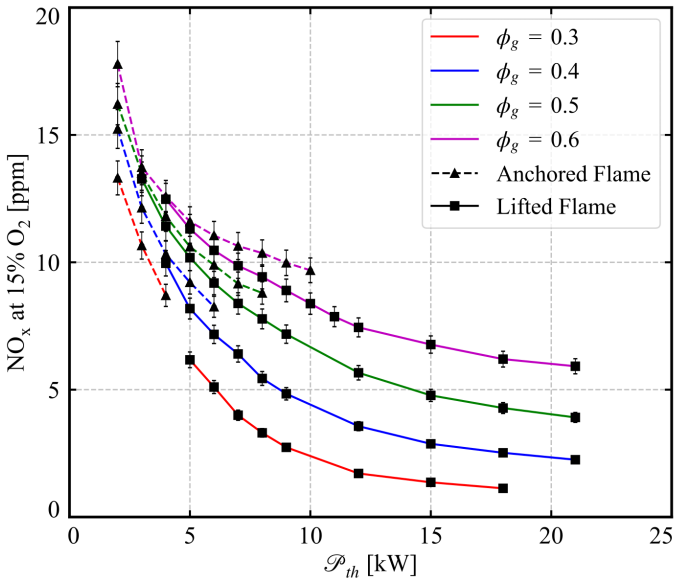

FIGURE 7: NO_x emissions as a function of the input thermal power $\mathscr{P}_{th}$ for different global equivalence ratios ϕ_g when air is injected at ambient temperature $T_{air,in} = T_{amb}$.

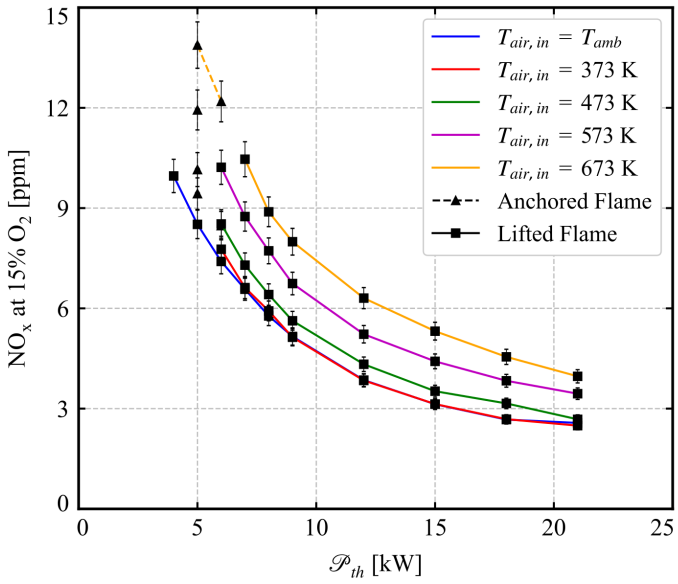

FIGURE 8: NO_x emissions as a function of the input thermal power $\mathscr{P}_{th}$ for different air preheating levels at constant equivalence ratio $\phi_g = 0.4$.

the increase of $T_{air,in}$, suggesting larger burning rates. While increasing the air inlet temperature $T_{air,in}$ produces more compact flames, the stabilization mode in Zone 3 remains however unchanged. At least for the operating conditions considered, the flames remain lifted over a span of air inlet temperatures of technical interest.

NO_x EMISSIONS

NO_x are collected at the chamber outlet using the gas analyzer probe. Measurements are performed after the combustor has reached global thermal equilibrium determined by the inertia of the metallic walls. Thermocouples inserted at different locations in the metal are used to check that thermal equilibrium has been reached. It typically takes 20 minutes after ignition in the worst cases.

NO_x concentrations in ppm (at 15% O_2) are reported in Fig. 7 as a function of the global equivalence ratio ϕ_g and thermal power $\mathscr{P}_{th}$ when the air inlet temperature is kept at ambient conditions T_{amb}. Operating conditions with $\phi_g < 0.3$ are not considered in this study due to the significant amount of unburned H_2 present in the exhaust gases. The square markers denote lifted flames. Triangles correspond to anchored flames. At low thermal powers $\mathscr{P}_{th}$, flames are anchored at all global equivalence ratios. For thermal powers higher than $\mathscr{P}_{th} = 12$ kW, flames are always lifted due to the higher air and H_2 injection velocities that favor flame detachment. Nevertheless, there is a range of thermal powers for which flames undergo two possible stabilization modes, which also depends on the selected equivalence ratio. For $\phi_g = 0.6$, flames can be attached or lifted for $5\text{ kW} \leq \mathscr{P}_{th} \leq 10\text{ kW}$.

Overall, NO_x emissions increase when the global equivalence ratio ϕ_g increases from 0.3 to 0.6 due to the rise of the flame temperature that promotes the formation of NO_x in the burnt gases through the thermal Zeldovich route. More interestingly, Fig. 7 also shows that NO_x emissions reduce regularly by increasing the thermal power, regardless of the global equivalence ratio and irrespective of the flame stabilization regime. NO_x concentrations tend towards a plateau for high thermal powers which appears to be only a function of global equivalence ratio. A thorough analysis of this behavior would require to scrutinize the structure of the reaction layers, which is out of the scope of this study. However, hypotheses can be made to interpret these results. For the thermal NO_x route, emissions mainly depend on the adiabatic flame temperature. Thermal NO_x are formed in zones where the temperature is greater than 1800 K [32] and the residence time in these zones will determine the NO_x concentrations. Hence, higher injection velocities leading to a lower residence time could explain the decrease of NO_x emissions when the thermal power increases. Nevertheless, other reasons can also be identified. In case of separate injections of air and hydrogen, the flame temperature depends on the local combustion mode. For diffusion reaction layers, such as branch I of lifted flames and branches I and II for anchored flames, higher injection velocities lead to higher strain rates along these diffusion reaction layers, which become thinner and reduce their temper-

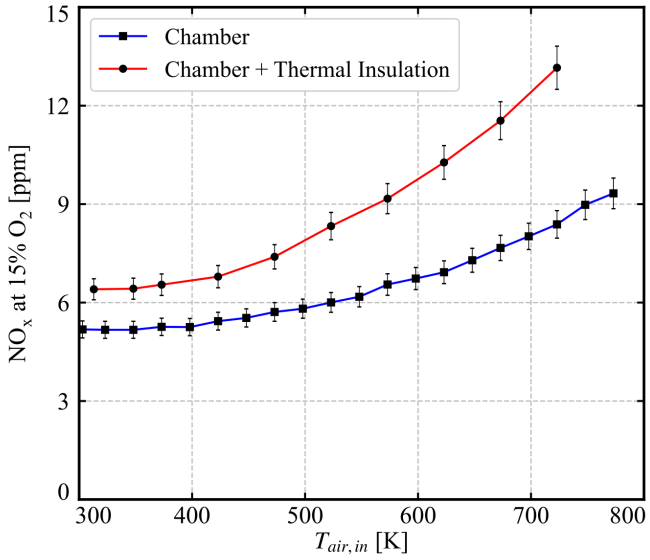

FIGURE 9: Effect of air preheating on NO_x emissions for different heat losses through the combustion chamber at constant input thermal power $\mathscr{P}_{th} = 9$ kW and constant equivalence ratio $\phi_g = 0.4$.

ature [33]. This second mechanism also results in lower NO_x concentrations. Finally, for the partially premixed rich branch II, the flame temperature is linked to the local equivalence ratio ϕ that mainly depends on the mixing efficiency between the air and hydrogen streams. Additional experiments not shown here indicate that mixing between the air and hydrogen streams exhausting from the HYLON burner mainly depends on the velocity ratio between the air and hydrogen streams. When the equivalence ratio is kept constant as in these experiments, this velocity ratio remains unchanged too. Consequently, the observed reduction of NO_x emissions may probably not be attributed to a better mixing between the hydrogen and fuel streams. Finally, for the operating conditions leading either to anchored or lifted flames, NO_x emissions are lower when the flame is lifted. At very low powers, the NO_x levels become however comparable for lifted and anchored flames, like for instance at $\mathscr{P}_{th} = 4$ kW for $\phi_g = 0.4$ and $\phi_g = 0.5$.

The impact of air-preheating on NO_x emissions is now investigated by keeping constant the global equivalence ratio to $\phi_g = 0.4$. Figure 8 plots the NO_x concentrations in ppm against the input thermal power $\mathscr{P}_{th}$ for air-inlet temperatures ranging from $T_{amb} = 293$ K to $T_{air,in} = 673$ K. A similar trend is observed as in Fig. 7 obtained for air injected at ambient conditions. Increasing the power, NO_x concentrations decrease regularly towards a plateau, reaching a value below 5.0 ppm regardless of the air pre-heated temperature. NO_x levels measured at T_{amb} and $T_{air,in} = 373$ K are close and only a further increase of the air inlet

TABLE 4: Evaluation of the global Wall Heat Losses (WHL) through the combustion chamber walls for different levels of air preheating at constant input thermal power $\mathscr{P}_{th} = 9$ kW and fixed equivalence ratio $\phi_g = 0.4$. Experiments with the standard combustion chamber (Ch.) and with the additional insulation layer around the chamber walls (Ch. + T.I.) are compared.

	$T_{air,in}$ [K]	T_{amb}	373	473	573	673
	T_{ad} [K]	1430	1484	1558	1633	1708
Ch.	T_{gb} [K]	1194	1216	1255	1293	1334
	WHL [kW]	1.8	2.0	2.3	2.7	3.0
Ch.	T_{gb} [K]	1349	1376	1417	1477	1517
+ T.I.	WHL [kW]	0.6	0.8	1.1	1.2	1.5
WHL ratio		-66%	-60%	-53%	-54%	-49%

temperature marks a detectable increase. Overall, NO_x emissions only slightly increase when the air inlet temperature increases from T_{amb} and $T_{air,in} = 673$ K. This is consistent with the NO_x dependence on the flame temperature [34]. Moreover, increasing the air inlet temperature $T_{air,in}$ only alters the flame stabilization regime at low power. For example, increasing the air inlet temperature from T_{amb} to 473 K at $\mathscr{P}_{th} = 6$ kW favors a transition from a lifted to an anchored flame. But, when $\mathscr{P}_{th} \geq 6$ kW the flame stabilization regime becomes insensitive to the air injection temperature $T_{air,in}$, confirming the results presented in Fig. 6. As a consequence, the gap in the NO_x production is only the consequence of the air preheating and does not dependent on the way the flame is stabilized.

Figure 9 shows how NO_x emissions increase with the air preheat temperature $T_{air,in}$ at a fixed global equivalence ratio $\phi_g = 0.4$ and given thermal power $\mathscr{P}_{th} = 9$kW. Results are compared for two different insulations of the combustion chamber, leading to different heat losses from the exhaust gases leaving the combustor. The blue line corresponds to the results with four quartz windows. The red line corresponds to a chamber insulated with a refractory fiber ceramic shell. The global wall heat losses (WHL) for each condition are estimated in Tab. 4 by comparing the adiabatic flame temperature T_{ad} with the temperature T_{gb} at the chamber outlet. The adiabatic temperature T_{ad} is calculated for a mixture featuring the global equivalence ratio. The results indicate an increasing dependence of NO_x emissions on WHL when air is preheated. At ambient conditions, 66% reduction in WHL leads to only a 23% increase in NO_x emissions, suggesting that most NO_x are formed in zones where WHL have a weak impact, such as in flame fronts or in the CRZ, where the local temperature is high [25]. The contribution from the outer recir-

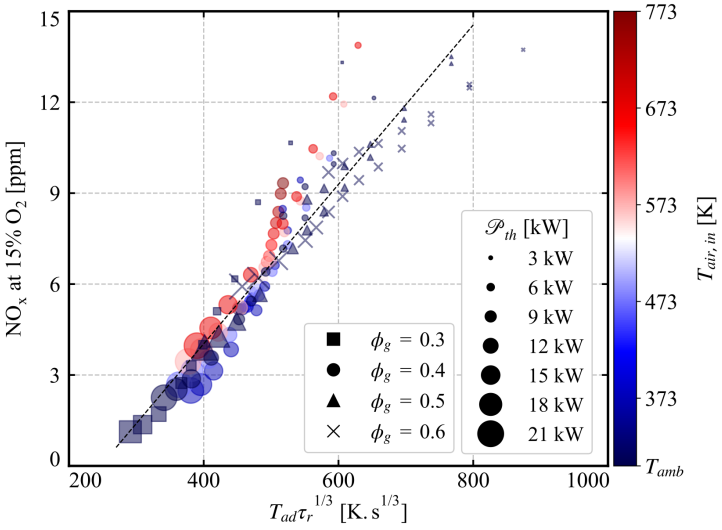

FIGURE 10: Distribution of NO_x emissions with respect to the product between the adiabatic flame temperature T_{ad} and the global residence time in the combustion chamber τ_r raised to the power 1/3. The entire experimental dataset is reported.

culation region and from the post-flame region, which are more sensitive to WHL, may explain the weak elevation of the difference in NO_x emissions that increase with air preheating. For example, a 57% increase in NO*x* emissions is observed with a 49% reduction in WHL at $T_{air,in} = 723$ K. Further experiments are needed to better evaluate the impact of WHL.

NO_x emissions can here be scaled with the flame temperature T_{ad} and the residence time τ_r of the burnt gases inside the combustor, which are known to determine NO_x emissions formed by the Zeldovich pathway [35–37]. The adiabatic flame temperature T_{ad} directly affects NO_x formation in the flame front and can also impact post-flame regions depending on the residence time τ_r. Oh *et al.* [36] identified a relationship between NO_x and $\tau_r^{1/2.8}$ for a fixed equivalence ratio. A similar relation is considered and tested in Fig. 10 using the entire set of data with the combustion chamber equipped with quartz windows. Different estimates of the residence time τ_r can be used. Hwang *et al.* [37] use the residence time of the hot gases in the flame volume [37]. Leroy *et al.* [24] used the residence time of the flow in the entire combustion chamber. The second approach is retained here by assuming that it is proportional to the effective residence time in high temperature regions:

$$\tau_r = L_q S_q \rho_b / (\dot{m}_{air} + \dot{m}_{H_2}) \tag{2}$$

where L_q is the chamber length, S_q is the square cross section area of the chamber and ρ_b is the density of burned gases calculated by 1D Cantera simulations. Fig. 10 shows that NO*x* emissions scale with $T_{ad}\tau_r^{1/3}$, especially at high thermal power for lifted flames, which have lower local flame temperatures close to T_{ad}. Departure from the scaling law are also observed for anchored flames in the upper right part in Fig. 10. This may be consequent to the reduction of the strain rate leading to an increase of the local flame temperature in diffusion reaction layers and higher NO_x emissions, as observed in [37].

Finally, Figs. 7 and 8 show that NO_x emissions remain globally low even at $T_{air,in} = 723$ K, where NO_x remain below 15 ppm. These emission levels should be compared to those measured for rupture low-NO_x technologies like micromix systems [7, 10, 11] or premixed and technically premixed hydrogen injectors [15, 38]. Operating the HYLON burner to ultra lean conditions with $\phi_g \leq 0.3$ yields to a further abatement of NO_x emissions.

CONCLUSION

The swirled HYLON injector operating with globally lean hydrogen/air mixtures has been tested with air injected at ambient temperature and with preheated air in a test rig at atmospheric pressure. Two flame archetypes have been observed. The first one is anchored to the hydrogen nozzle increasing the thermal load on this component. This burning mode is favored by the high reactivity of hydrogen. The second mode leads to aerodynamically stabilized flames with a low thermal stress on the burner.

It has been shown that the HYLON operability chart can be split in three zones. For low air and low hydrogen flow rates, the flame remains unconditionally anchored to the injector lips (Zone I). When the hydrogen injection velocity increases, the flame can be either anchored or lifted above the hydrogen injector lips depending on the path followed to reach the operating condition (Zone II). For high air flow rates, the flame is always lifted regardless of the path followed to reach the chosen operating condition (Zone III).

Flame transitions between these different zones have been determined together with the impact of the air inlet temperature up to 770 K. It was demonstrated that the size of Zone 1 is controlled by the increase of the edge flame velocity with the air preheat temperature. However, air preheating has minimal effect on Zone III, despite a reduction in flame size due to the increased reactivity of the preheated flames.

NO_x emissions have been measured for increasing thermal powers at different global equivalence ratios. Slight differences on NO_x emissions are observed between the two stabilization modes but the emissions drop when the thermal power increases. The same trend is observed when air is preheated. For the lean operating conditions investigated, and regardless of the wall chamber heat losses, NO_x concentrations remain low for all operating conditions tested. For instance, at $\phi_g = 0.4$, NO_x emissions at 15% O_2 molar fraction remain in all cases below 15 ppm even

for air preheated up to $T_{air,in} = 770$ K. Finally, it was shown that NO_x emissions scale with the product of the adiabatic flame temperature T_{ad} and chamber residence time τ_r raised to the power $1/3$.

These experiments indicate that the HYLON injector has promising characteristics in terms of flame stabilization, low thermal stress and NO_x emissions for aerojet engines. It enables to stabilize lifted flames over a wide range of operating conditions with flames that are barely affected by air preheating. However, additional investigations must be carried out to investigate its performance at higher pressures and higher Reynolds numbers to get closer to engine like conditions.

ACKNOWLEDGMENT

This project has received funding from the European Research Council under the European Union's Horizon 2020 research and innovation program Grant Agreement 832248, SCIROCCO. The authors are grateful to the technical support from G. Albert, S. Lun Kwong Leon and L. Mouneix from IMFT.

REFERENCES

[1] Sánchez, A. L., and Williams, F. A., 2014. "Recent advances in understanding of flammability characteristics of hydrogen". *Progress in Energy and Combustion Science,* ***41***(1), pp. 1–55.

[2] Yahou, T., Dawson, J. R., and Schuller, T., 2023. "Impact of chamber back pressure on the ignition dynamics of hydrogen enriched premixed flames". *Proceedings of the Combustion Institute,* ***39***(4), pp. 4641–4650.

[3] ETNGlobal, 2020. Hydrogen Gas Turbines: The Path Towards a Zero-Carbon Gas Turbine. Tech. rep.

[4] Skottene, M., and Rian, K. E., 2007. "A study of NOx formation in hydrogen flames". *International Journal of Hydrogen Energy,* ***32***(15 SPEC. ISS.), pp. 3572–3585.

[5] Du Toit, M. H., Avdeenkov, A. V., and Bessarabov, D., 2018. "Reviewing H2 Combustion: A Case Study for Non-Fuel-Cell Power Systems and Safety in Passive Autocatalytic Recombiners". *Energy and Fuels,* ***32***(6), pp. 6401–6422.

[6] Dodo, S., Asai, T., Koizumi, H., Takahashi, H., Yoshida, S., and Inoue, H., 2011. "Combustion characteristics of a multiple-injection combustor for dry low-NOx combustion of hydrogen-rich fuels under medium pressure". *ASME J. Eng. Gas Turbines Power,* ***2***, Jun., pp. 467–476.

[7] Hernandez, S. R., Wang, Q., McDonell, V., Mansour, A., Steinthorsson, E., Hollon, B., and Hannifin, P., 2008. "Micro-mixing fuel injectors for low emissions hydrogen combustion". *ASME J. Eng. Gas Turbines Power,* ***3***, Aug., pp. 675–685.

[8] Funke, H., Beckman, N., Keinz, J., and Horikawa, A., 2020. "30 years of dry low nox micromix combustor research for hydrogen-rich fuels: An overview of past and present activities". *ASME J. Eng. Gas Turbines Power,* ***6***, Sep., p. 13213.

[9] York, W. D., Ziminsky, W. S., and Yilmaz, E., 2013. "Development and testing of a low NOx hydrogen combustion system for heavy-duty gas turbines". *ASME J. Eng. Gas Turbines Power,* ***135***(2), Feb., p. 022001.

[10] Marek, C., Smith, T., and Kundu, K., 2005. "Low emission hydrogen combustors for gas turbines using lean direct injection". In 41st AIAA/ASME/SAE/ASEE joint propulsion conference & exhibit, p. 3776.

[11] Haj Ayed, A., Kusterer, K., Funke, H., Keinz, J., Striegan, C., and Bohn, D., 2015. "Improvement study for the dry-low-NOx hydrogen micromix combustion technology". *Propulsion and Power Research,* ***4***(3), Sep., pp. 132–140.

[12] Syred, N., and Beér, J. M., 1974. "Combustion in swirling flows: A review". *Combustion and Flame,* ***23***(2), Oct., pp. 143–201.

[13] Choi, J., Ahn, M., Kwak, S., Lee, J. G., and Yoon, Y., 2022. "Flame structure and NOx emission characteristics in a single hydrogen combustor". *International Journal of Hydrogen Energy,* ***47***(68), pp. 29542–29553.

[14] Claypole, T., and Syred, N., 1981. "The effect of swirl burner aerodynamics on nox formation". In Symposium (International) on Combustion, Vol. 18, Elsevier, pp. 81–89.

[15] Reichel, T. G., Terhaar, S., and Paschereit, C. O., 2013. "Flow field manipulation by axial air injection to achieve flashback resistance and its impact on mixing quality". In 43rd AIAA Fluid Dynamics Conference, p. 2603.

[16] Capurso, T., Laera, D., Riber, E., and Cuenot, B., 2023. "NOx pathways in lean partially premixed swirling H2-air turbulent flame". *Combustion and Flame,* ***248***, p. 112581.

[17] Chterev, I., and Boxx, I., 2021. "Effect of hydrogen enrichment on the dynamics of a lean technically premixed elevated pressure flame". *Combustion and Flame,* ***225***, pp. 149–159.

[18] Cheng, R. K., Littlejohn, D., Strakey, P. A., and Sidwell, T., 2009. "Laboratory investigations of a low-swirl injector with H2 and CH4 at gas turbine conditions". *Proceedings of the Combustion Institute,* ***32 II***(2), pp. 3001–3009.

[19] Richard, S., Viguier, C., Marragou, S., and Schuller, T., 2021. *Dispositif d'injection de dihydrogène et d'air (FR Patent No FR2111267)*. Institut National de la Propriété Industrielle.

[20] Marragou, S., Magnes, H., Poinsot, T., Selle, L., and Schuller, T., 2022. "Stabilization regimes and pollutant emissions from a dual fuel CH4/H2 and dual swirl low NOx burner". *International Journal of Hydrogen Energy,*

47(44), May, pp. 19275–19288.

[21] Yuasa, S., 1986. "Effects of swirl on the stability of jet diffusion flames". *Combustion and Flame,* ***66***(2), pp. 181–192.

[22] Degeneve, A., Mirat, C., Caudal, J., Vicquelin, R., and Schuller, T., 2019. "Effects of Swirl on the Stabilization of Non-Premixed Oxygen-Enriched Flames above Coaxial Injectors". *ASME J. Eng. Gas Turbines Power,* ***141***(12), Dec., p. 121018.

[23] Degeneve, A., Vicquelin, R., Mirat, C., Caudal, J., and Schuller, T., 2021. "Impact of co- And counter-swirl on flow recirculation and liftoff of non-premixed oxy-flames above coaxial injectors". *Proceedings of the Combustion Institute,* ***38***(4), Dec., pp. 5501–5508.

[24] Leroy, M., Mirat, C., Renaud, A., and Vicquelin, R., 2023. "Stabilization of Low-Nox Hydrogen Flames On a Dual-Swirl Coaxial Injector". *ASME J. Eng. Gas Turbines Power,* ***145***(2), Feb., p. 021021.

[25] Aniello, A., Laera, D., Marragou, S., Magnes, H., Selle, L., Schuller, T., and Poinsot, T., 2023. "Experimental and numerical investigation of two flame stabilization regimes observed in a dual swirl h2-air coaxial injector". *Combustion and Flame,* ***249***, p. 112595.

[26] Marragou, S., Magnes, H., Aniello, A., Selle, L., Poinsot, T., and Schuller, T., 2023. "Experimental analysis and theoretical lift-off criterion for h2/air flames stabilized on a dual swirl injector". *Proceedings of the Combustion Institute,* ***39***(4), pp. 4345–4354.

[27] Brohez, S., Delvosalle, C., and Marlair, G., 2004. "A two-thermocouples probe for radiation corrections of measured temperatures in compartment fires". *Fire Safety Journal,* ***39***, pp. 399–411.

[28] Price, R., Hurle, I., and Sugden, T., 1969. "Optical studies of the generation of noise in turbulent flames". In Symposium (international) on combustion, Vol. 12, Elsevier, pp. 1093–1102.

[29] Schefer, R. W., Kulatilaka, W. D., Patterson, B. D., and Settersten, T. B., 2009. "Visible emission of hydrogen flames". *Combustion and Flame,* ***156***(6), pp. 1234–1241.

[30] Muñiz, L., and Mungal, M. G., 1997. "Instantaneous flame-stabilization velocities in lifted-jet diffusion flames". *Combustion and Flame,* ***111***(1-2), pp. 16–30.

[31] Joedicke, A., Peters, N., and Mansour, M., 2005. "The stabilization mechanism and structure of turbulent hydrocarbon lifted flames". *Proceedings of the Combustion Institute,* ***30***(1), pp. 901–909.

[32] Steele, R. C., Malte, P. C., Nicol, D. G., and Kramlich, J. C., 1995. "Nox and n2o in lean-premixed jet-stirred flames". *Combustion and Flame,* ***100***(3), pp. 440–449.

[33] Lee, S.-R., Park, S.-S., and Chung, S.-H., 1995. "Flame structure and thermal no x formation in hydrogen diffusion flames with reduced kinetic mechanisms". *KSME Journal,* ***9***, pp. 377–384.

[34] Frassoldati, A., Faravelli, T., and Ranzi, E., 2006. "A wide range modeling study of NOx formation and nitrogen chemistry in hydrogen combustion". *International Journal of Hydrogen Energy,* ***31***(15), Dec., pp. 2310–2328.

[35] Tuncer, O., Acharya, S., and Uhm, J. H., 2009. "Dynamics, NOx and flashback characteristics of confined premixed hydrogen-enriched methane flames". *International Journal of Hydrogen Energy,* ***34***(1), pp. 496–506.

[36] Oh, J., Hwang, J., and Yoon, Y., 2010. "EINOx scaling in a non-premixed turbulent hydrogen jet with swirled coaxial air". *International Journal of Hydrogen Energy,* ***35***(16), Aug., pp. 8715–8722.

[37] Hwang, J., Sohn, K., Bouvet, N., and Yoon, Y., 2013. "NOx Scaling of Syngas H2/CO Turbulent Non-Premixed Jet Flames". *Combustion Science and Technology,* ***185***(12), pp. 1715–1734.

[38] Brunetti, I., Riccio, G., Rossi, N., Cappelletti, A., Bonelli, L., Marini, A., Paganini, E., and Martelli, F., 2011. "Experimental and numerical characterization of lean hydrogen combustion in a premix burner prototype". In Turbo Expo: Power for Land, Sea, and Air, Vol. 54624, pp. 601–612.